Nano Research

Open Access

Research Article

# Elucidating the nexus between Fe coordination and N-doped carbon matrix for efficient oxygen reduction catalysts

Xiaokai Ding[1,§], Hang Lei[1,§] ✉, Xi Luo[1], Kun Yu[3], Wenbiao Zhang[3], Lu-Lu Zhang[1] ✉, Xue-Lin Yang[1], Lei Li[2] ✉, Zhan Lin[2], and Wenjie Mai[4] ✉

[1] *Hubei Provincial Collaborative Innovation Center for New Energy Microgrid, College of Electrical Engineering & New Energy, China Three Gorges University, Yichang 443002, China*
[2] *School of Chemical Engineering and Light Industry, Guangdong University of Technology, Guangzhou, 510006, China*
[3] *College of Chemistry and Materials Science, and Guangdong Provincial Key Laboratory of Functional Supramolecular Coordination Materials and Applications, Jinan University, Guangzhou 510632, China*
[4] *Siyuan Laboratory, Guangzhou Key Laboratory of Vacuum Coating Technologies and New Energy Materials, Guangdong Provincial Engineering Technology Research Center of Vacuum Coating Technologies and New Energy Materials, College of Physics and Optoelectronic Engineering, Jinan University, Guangzhou 510632, China*
[§] *Xiaokai Ding and Hang Lei contributed equally to this work.*

**Cite this article:** *Nano Research*, **2026**, *19*, 94908471. https://doi.org/10.26599/NR.2026.94908471

**ABSTRACT:** In the pursuit of inexpensive and efficient oxygen reduction catalysts, Fe–N–C catalysts have garnered significant attention as a viable alternative to scarce platinum-based materials. Nevertheless, the intricate interaction between the carbon matrix and Fe active sites, along with the mechanism by which such synergies modulate catalytic activity, remains elusive. Herein, a programmed temperature pyrolysis strategy is developed to optimize both the carbon matrix properties and coordination environments of Fe sites. Systematic characterizations uncover the correlations between key parameters of Fe sites (the oxidation state, coordination number, and density of state), as well as the carbon matrix (the functional groups, nitrogen species and content, and the degree of graphitization), with the resultant catalytic activity. The optimized catalyst exhibits a high half-wave potential of 0.935 V and good stability, and the assembled zinc–air battery delivers a high peak power density and long-term cycling durability. Theoretical calculations reveal that Fe–$N_4$ coordination more effectively reduces the energy barrier for *OH release compared to Fe–$N_3$ coordination. Additionally, adjacent graphitic nitrogen species further lower the energy barrier of the rate-determining step, thereby accelerating oxygen reduction kinetics. This work highlights the critical role of the carbon support and Fe site properties in synergistically boosting the catalytic performance.

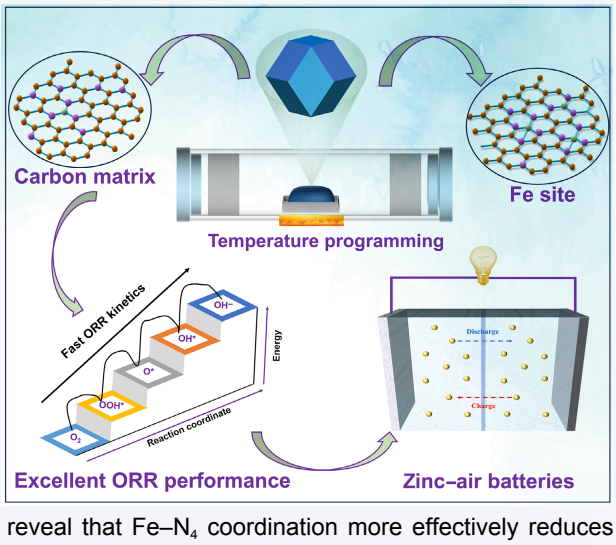


**KEYWORDS:** Fe coordination, carbon matrix, oxygen reduction reaction, Fe–N–C catalysts, zinc–air battery

## 1 Introduction

The oxygen reduction reaction (ORR) is of paramount significance, with applications spanning a broad spectrum of fields [1]. These include energy-related domains, such as fuel cells and metal–air batteries, as well as environmental-focused areas, and industrial production-oriented sectors [2]. Among these, zinc–air batteries (ZABs) are characterized by their high energy density, low cost, environmental friendliness, high safety, and ultra-long cycle life, endowing them with vast application potential across various fields [3, 4]. However, the large-scale commercialization of ZABs, whose air cathode depends on Pt-based catalysts to drive the ORR, is impeded by the exorbitant cost, limited availability, subpar stability,

**Received:** November 12, 2025; **Revised:** December 26, 2025
**Accepted:** January 21, 2026

✉Address correspondence to Lu-Lu Zhang, luluzhang@ctgu.edu.cn; Hang Lei, leihang@ctgu.edu.cn; Lei Li, li.lei@gdut.edu.cn; Wenjie Mai, wenjiemai@email.jnu.edu.cn

and intricate preparation procedures associated with Pt [5–7]. Thus, it is imperative to conduct further in-depth research and innovation to develop inexpensive and efficient ORR catalysts.

Extensive research has established Fe–N–C catalysts as highly promising alternatives to the precious metal Pt for the ORR, with $FeN_4$ being identified as the local atomic coordination structure of the metal center [8, 9]. Current research on Fe–N–C single-atom catalysts primarily focuses on the regulation of Fe species, their coordination environment, and the modulation of electronic state through tailoring the Fe coordination environment [10, 11]. However, the role of Fe–N–C single-atom catalysts in catalysis should extend beyond the mere involvement of $Fe–N_4$ sites or merely provide support for the catalytic process [12]. In other words, $Fe–N_4$ sites should not be regarded as the sole determinant or the only active participants in catalysis; the proportion, type, and bonding configuration of each element in the N-doped carbon matrix also exert a significant influence on catalytic performance [13]. To elucidate the source of catalytic activity in Fe–N–C single-atom catalysts, where Fe atoms are highly dispersed on an N-doped carbon matrix via Fe–N bonds, two key perspectives must be considered: the $FeN_4$ site and the nitrogen-doped carbon substrate. The $FeN_4$ site is associated with the spatial arrangement and coordination environment, as well as charge distribution and orbital configuration [14]. The nitrogen-doped carbon substrate, on the other hand, encompasses carbon defects and edges, N species, graphite carbon content, and surface functional groups. Parsing these complementary aspects enables a comprehensive understanding of the active sites and reaction mechanisms, ultimately guiding the precise design of Fe–N–C catalysts. Neglecting these aspects would result in an incomplete understanding of active sites, restrict elucidation of the reaction mechanisms, and hinder advancement in catalyst design and optimization [15]. However, the synergistic effect of the $FeN_4$ site and the nitrogen-doped carbon substrate on catalytic activity remains unclear due to a lack of in-depth and systematic research. Therefore, optimizing the properties of both the $FeN_4$ site and the N-doped carbon matrix through a controllable synthesis process is of great significance for enhancing the activity of Fe–N–C catalysts and clarifying the catalytic mechanism.

Herein, we precisely regulated the carbonization process of Fe-doped zeolitic imidazolate framework-8 (ZIF-8) precursors via temperature programming, thereby tailoring the properties of the $FeN_4$ site and the N-doped carbon matrix, and successfully fabricated a series of Fe–N–C catalysts. The enhancement of catalytic activity is predominantly modulated through the optimization of the programmed temperature annealing process. The optimized Fe-500-40 (Fe-doped ZIF-8 annealed at intermediate heat-treatment temperature of 500 °C for 40 min was labeled Fe-500-40) catalyst exhibits an impressive half-wave potential ($E_{1/2}$) of 0.935 V, a low Tafel slope of 63.69 mV·dec$^{-1}$, and excellent stability. Fe-500-40-based ZABs deliver high peak power density and outstanding long-term durability. Combined systematic characterization and theoretical calculations reveal that the Fe sites and the carbon matrix synergistically act to markedly boost ORR catalytic activity. By elucidating the intrinsic relationship between Fe sites and the carbon matrix in Fe–N–C catalysts, this work provides critical insights, laying a foundation for the rational design of practical metal–N–C catalysts.

## 2 Results and discussion

The properties of the $FeN_4$ site and the N-doped carbon matrix in Fe–N–C catalysts are primarily determined by the selection of suitable precursors and the optimization of pyrolysis conditions. As depicted in the schematic diagram (Fig. 1(a)), the Fe–N–C catalysts, derived from the annealing of Fe-doped ZIF under varying conditions, exhibit marked variations in the composition and structure of both Fe sites and the carbon matrix. A series of Fe–N–C catalysts (denoted as Fe–*X*–*Y*) was synthesized by adjusting the calcination time (*Y*) at the intermediate heat-treatment temperature (*X*). Specifically, *Y* was set to 20, 40, or 60 min, and *X* was 400, 500, or 600 °C. The catalysts were named based on their annealing parameters. To obtain dispersed Fe single atoms and promote the volatilization of Zn elements, all catalysts were heated to 1000 °C and maintained for 1 h, and detailed experimental steps are provided in Section S1 in the Electronic Supplementary Material (ESM). Subsequently, we conducted comprehensive compositional and microstructural analyses on both the precursor and the annealed products. X-ray diffraction (XRD) patterns (Fig. S1 in the ESM) indicate that the Fe-doped ZIF-8 retains the identical phase composition as pristine ZIF-8. Scanning electron microscopy (SEM) and transmission electron microscopy (TEM) images show that Fe-doped ZIF-8 exhibits a typical octahedral structure, confirming the successful integration of Fe into the ZIF-8 framework (Fig. S2 in the ESM). Thermogravimetric analysis displays that both ZIF-8 and Fe-doped ZIF-8 undergo the first stage of framework collapse within the temperature range of 300–500 °C (Fig. S3 in the ESM). Furthermore, *in situ* heating XRD was employed to investigate the phase evolution of Fe-doped ZIF-8 at different temperatures. Below 400 °C, Fe-doped ZIF-8 essentially maintains its original crystal structure (Fig. 1(b)). However, at 400–900 °C, Fe-doped ZIF-8 experiences a substantial phase transformation, beginning to convert into zinc oxide and other impurity phases [16]. Above 900 °C, Fe and $FeN_x$ species are formed, and Zn-related species volatilize at high temperatures [17]. Similarly, the phase transformation trends of Fe-doped ZIFs are basically consistent when they stay at the intermediate temperature for a specific constant temperature time (Fig. S4 in the ESM). Phase analyses of acid-washed products (Fig. 1(c)) indicate that the diffraction peaks at about 23° and 43° are assigned to the (002) and (100) planes of graphitic carbon, respectively, with no other crystalline phases detected [18]. The purpose of acid washing is to remove elemental Fe while leaving $FeN_x$ species. Additionally, variations in annealing conditions alter the position and intensity of these (002) and (100) crystal planes, thereby confirming the feasibility of regulating the carbon matrix composition through temperature-controlled annealing.

To further clarify how annealing conditions affect nanostructures, we systematically analyzed the morphological changes induced by varying calcination parameters. As revealed by the SEM and TEM images (Figs. S5–S11 in the ESM), the microstructures of both ZIF-8 and Fe-doped ZIF-8 undergo varying degrees of collapse following calcination under different conditions. High-resolution TEM images further confirm that the calcined catalysts partially retain the octahedral morphology inherent to pristine ZIF-8. The morphology of ZIF-8-derived catalysts after calcination varies slightly under different conditions, primarily because varying calcination conditions influence the redox reactions of metal nodes, the collapse of the metal framework, the formation of new crystal phases, the decomposition rate of organic ligands, and the interaction between Fe and Zn or ligands [19–21]. The nitrogen adsorption isotherms of Fe-400-40,

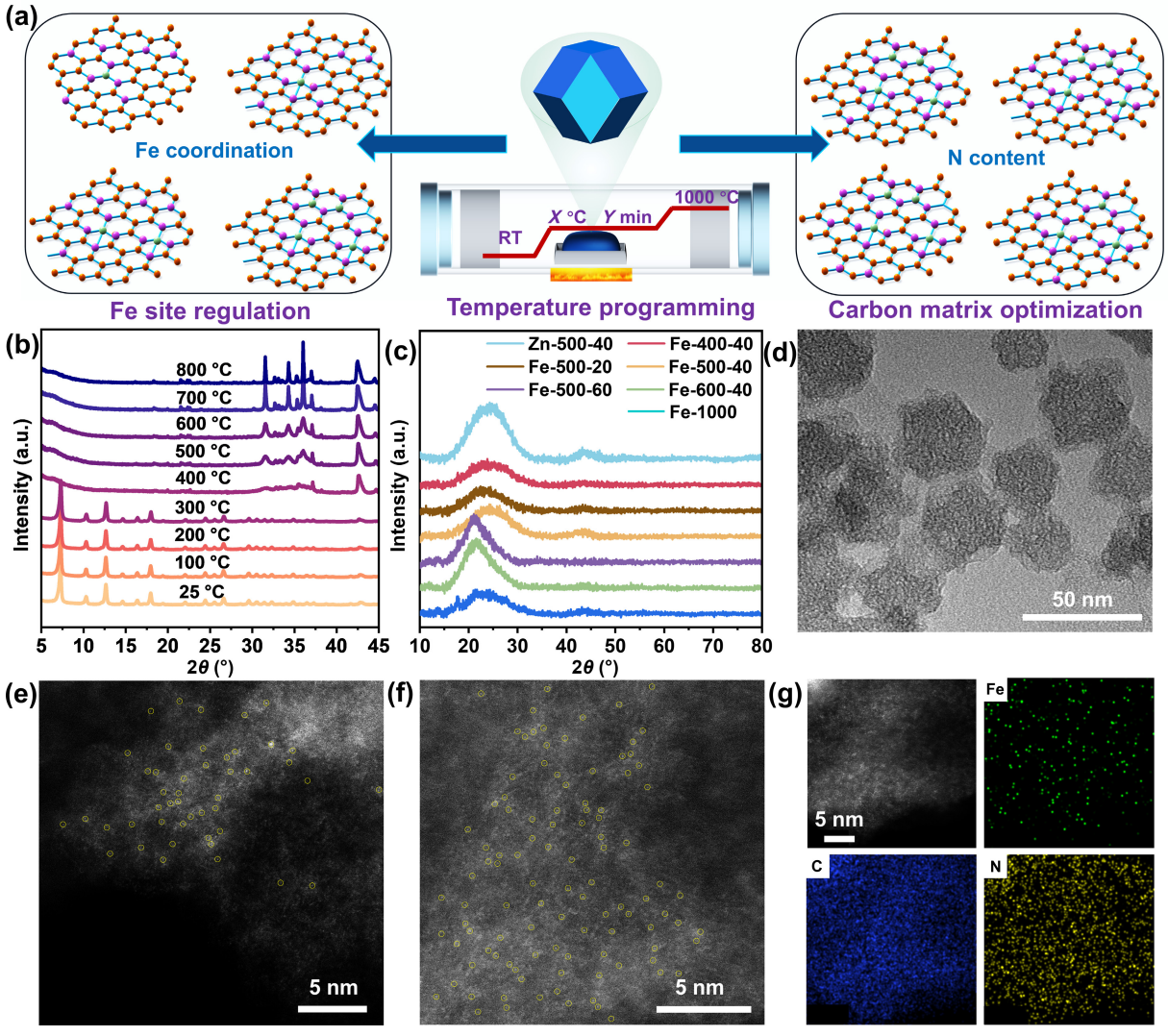


**Figure 1** (a) Schematic diagram of the preparation of various types of Fe–N–C catalysts by programmed temperature control. (b) *In situ* heating XRD patterns of Fe-doped ZIF-8. (c) the XRD patterns of various types of Fe–N–C catalysts. (d) TEM image of Fe-500-40. ((e) and (f)) Aberration-corrected atomic resolution HAADF-STEM micrograph of Fe-500-40, recorded in distinct regions, with individual Fe single atoms circled for clarity. (g) HAADF-STEM image and corresponding EDS mapping images.

Fe-500-40, and Fe-600-40 catalysts were analyzed to evaluate how variations in *X* influence surface area and pore-size distribution. As *X* increased, the total pore volume, average pore diameter, and the Brunauer–Emmett–Teller (BET) surface area of Fe-400-40, Fe-500-40, and Fe-600-40 catalysts showed a slight downward trend (Fig. S12 in the ESM). These changes are attributed to the accelerated collapse of the ZIF framework at higher intermediate heat-treatment temperatures [22]. Nevertheless, the isotherms display classic Type I curves with distinct plateaus, indicative of a predominantly microporous structure [23]. Additionally, pore-size distribution analysis reveals peaks between 0.5 and 20 nm, signifying the coexistence of micropores and small mesopores, with the overall distribution pattern remaining consistent across samples.

Furthermore, the Fe-500-40 catalyst was selected as a representative to specifically study the structural properties. As depicted in Fig. 1(d), the Fe-500-40 catalyst exhibits an irregular polyhedral morphology, with most primary catalyst particles measuring 30–40 nm in size. In Fig. 1(e), an aberration-corrected high-angle annular dark-field scanning TEM (HAADF-STEM) image clearly reveals that atomically dispersed Fe sites, which appear as bright dots distributed across the carbon skeleton. The Fe atoms are uniformly distributed throughout the entire carbon matrix. The strong signal intensity in the image indicates a high Fe loading (Fig. 1(f)), which was precisely quantified as 0.83 wt.% by inductively coupled plasma mass spectrometry (ICP-MS, Fig. S13 in the ESM) [1, 24, 25]. The extensive and uniform distribution of Fe atoms within the nitrogen-doped carbon matrix was further corroborated by energy-dispersive X-ray spectroscopy (EDS) elemental mapping (Fig. 1(g)).

The catalytic performance and stability of the synthesized Fe–N–C catalysts were systematically investigated. As evidenced by the linear sweep voltammetry (LSV) curve in 0.1 M KOH (Fig. 2(a)), there are pronounced differences in the activities of the Fe–N–C catalysts synthesized under varying calcination conditions. This observation indirectly corroborates that regulating $FeN_4$ active site and the N-doped carbon matrix exerts a substantial impact on catalytic performance. Notably, the Fe-500-40 catalyst exhibits the highest $E_{1/2}$ of 0.935 V, accompanied by a limiting current density of about 6 mA·cm$^{-2}$. It is noteworthy that the Fe-500-40 catalyst exhibits extremely superior activity compared to the commercial

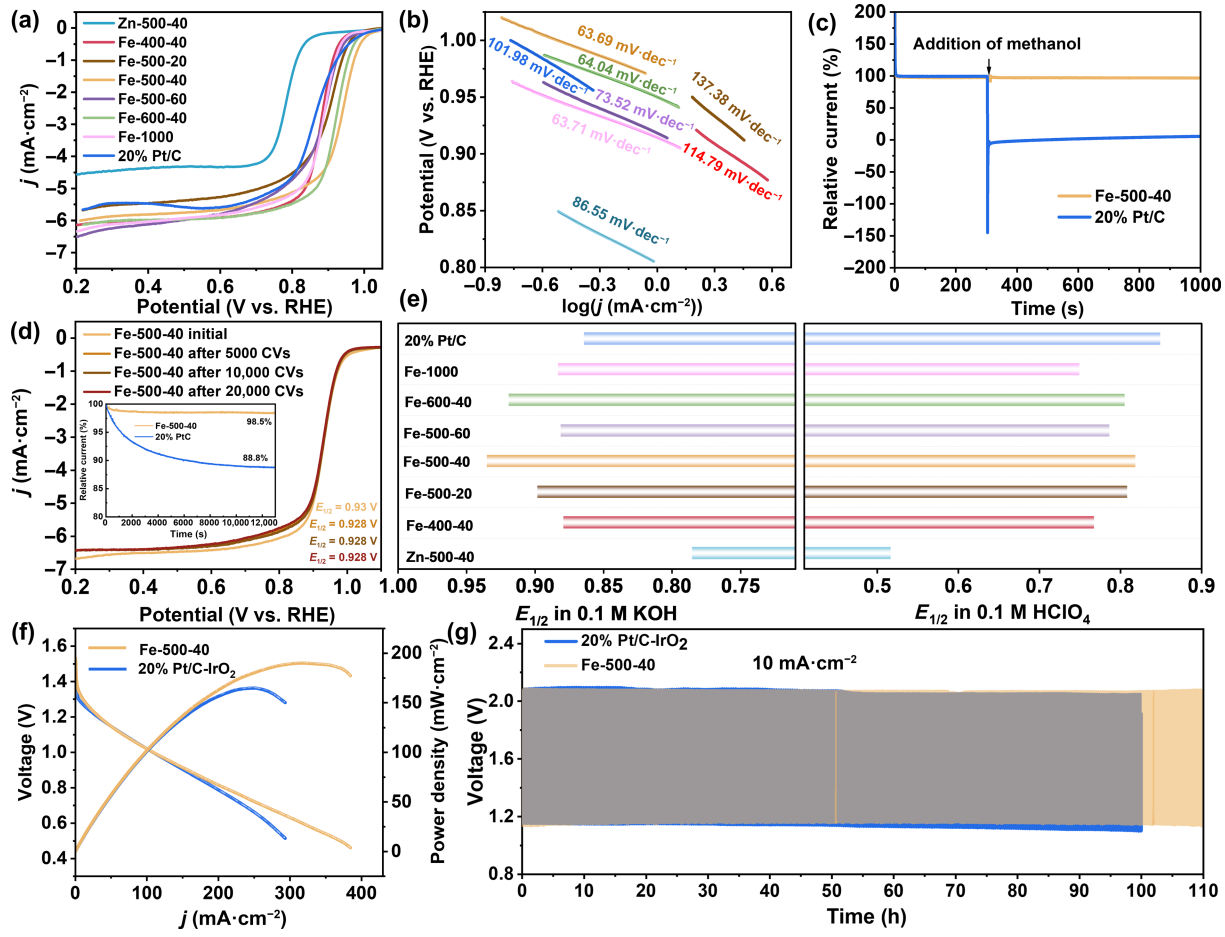


**Figure 2** (a) ORR polarization curves of various catalysts in 0.1 M KOH electrolyte. (b) The corresponding Tafel curves. (c) Methanol tolerance tests of Fe-500-40 and 20% Pt/C. (d) LSV of Fe-500-40 before and after various cycles stability test, inset is the chronoamperometric *i*–*t* plot of Fe-500-40 and 20% Pt/C. (e) Comparison of half-wave potentials of various catalysts in 0.1 M KOH and 0.1 M $HClO_4$ electrolytes. (f) Discharge polarization and power density curves of ZABs. (g) Galvanostatic discharge/charge curves at 10 mA·cm$^{-2}$ for ZABs with Fe-500-40 and 20% Pt/C-$IrO_2$.

20% Pt/C catalyst ($E_{1/2}$ = 0.864 V). The differences in the limiting diffusion current density are mainly affected by factors, such as oxygen diffusion rate, specific surface area, and porosity [26]. Corresponding Tafel plots (Fig. 2(b)) show that Fe-500-40 has a Tafel slope of 63.69 mV·dec$^{-1}$, indicating faster electron-transfer kinetics compared to other samples. Given that it is the excellent activity, methanol and $SCN^-$-poisoning experiments were performed to assess its stability. As depicted in Fig. 2(c), during methanol poisoning experiments conducted in an $O_2$-saturated 0.1 M KOH solution with 5% methanol introduced at time ($t$) = 300 s, the chronoamperometric curves reveal a sharp drop in current density for 20% Pt/C. In contrast, the Fe-500-40 catalyst exhibits no significant change, highlighting its remarkable methanol tolerance. It is well-established that the $SCN^-$ ion has a strong affinity for Fe and can effectively poison the Fe–$N_4$ coordination during ORR catalysis [27]. Upon adding 0.01 M KSCN to the $O_2$-saturated 0.1 M KOH solution, the half-wave potential of the Fe-500-40 catalyst experiences a minor negative shift of 10 mV (Fig. S14 in the ESM). After rinsing the electrode with water and conducting re-measurements in 0.1 M $O_2$-saturated KOH, it is observed that the ORR polarization curve reverts to its original state as the LSV tests progress. These findings unambiguously indicate that the Fe-500-40 catalyst possesses commendable anti-$SCN^-$ properties. The long-term durability of the Fe-500-40 catalyst was also evaluated. Following a series of accelerated cyclic voltammetry (CV) cycles (5000, 10,000, and 20,000), the $E_{1/2}$ of Fe-500-40 exhibited only a negligible decay (Fig. 2(d)). Additionally, the chronoamperometric current ($i$)–$t$ plot further demonstrated superior stability of Fe-500-40 compared to commercial 20% Pt/C (inserted in Fig. 2(d)).

It is worth highlighting that the Fe-500-40 catalyst not only demonstrates exceptional activity in alkaline solutions but also exhibits promising performance in acidic solutions (Fig. 2(e)). Among the evaluated catalysts, the Fe-500-40 achieves an $E_{1/2}$ of 0.819 V, which is second only to the 0.85 V of 20% Pt/C and surpasses the other tested catalysts (Fig. S15 in the ESM). Moreover, under alkaline conditions, the Fe-500-40 exhibits an oxygen evolution reaction (OER) overpotential of merely 382 mV at a current density of 10 mA·cm$^{-2}$ (Fig. S16(a) in the ESM). The potential difference ($\Delta E = E_{j=10} - E_{1/2}$, where $E_{j=10}$ represents the OER potential at a current density of 10 mA·cm$^{-2}$) serves as a crucial indicator of bifunctional OER/ORR activity [28]. To assess the bifunctional electrocatalytic properties of Fe-500-40, the LSV measurements were performed over a wide voltage window. As shown in Fig. S16(b) in the ESM, the Fe-500-40 catalyst achieves remarkable bifunctional activity with an indicator $\Delta E$ of 0.677 V. Leveraging its superior bifunctional catalytic activity, we further assembled aqueous alkaline ZABs using Fe-500-40. As illustrated

in Fig. S17(a) in the ESM, the Fe-500-40-based aqueous ZAB exhibited a significantly narrowed charge–discharge voltage gap and achieved a peak power density of 189.9 mW·cm$^{-2}$, outperforming the conventional 20% Pt/C-$IrO_2$-based ZAB (Fig. 2(f)). The specific capacity of the Fe-500-40-based ZAB, calculated based on the mass of consumed Zn, reached 765 mAh·g$^{-1}$ at a discharge current density of 10 mA·cm$^{-2}$ (Fig. S17(b) in the ESM). Furthermore, for long-term cycling performance evaluation, the Fe-500-40-based ZAB was subjected to cycling at a current density of 10 mA·cm$^{-2}$. As depicted in Fig. 2(g), after 110 h, the charge/discharge voltage gap remained virtually unchanged, and the system still retained a high energy conversion efficiency of 54.5%. The discharge voltage of the 20% Pt/C-$IrO_2$-based ZAB gradually decreased after 30 cycles, and its energy conversion efficiency was approximately 52.8% after 100 cycles, confirming its poor cycling stability. The aforementioned electrochemical performances collectively confirm that temperature-programmed calcination serves as an effective strategy for modulating the catalytic performance of ZIF-8-derived catalysts, with Fe-500-40 emerging as the optimal catalyst in this series, exhibiting the highest catalytic activity and stability.

Furthermore, to elucidate the origin of catalytic activity and the regulatory mechanisms underlying the Fe–N–C catalyst series, the atomic coordination and electronic structure of Fe were meticulously analyzed by X-ray absorption spectroscopy (XAS). The Fe K-edge X-ray absorption near-edge structure (XANES) spectra reveal that the catalysts exhibit distinct near-edge absorptions compared to Fe foil, iron phthalocyanine (FePc), and $Fe_3O_4$ (Fig. 3(a)). Additionally, the Fe K-edge XANES spectra of the Fe–N–C catalyst series are akin to those of FePc and $Fe_3O_4$, indicating that the valence states of these catalysts lie between +2 and +3 oxidation states [29]. By correlating edge energy, oxidation state, and $E_{1/2}$ of the ORR for each catalyst, it was determined that the valence state of Fe primarily ranges from +2.5 to +2.8 (Figs. 3(b) and 3(c)). Among them, Fe-500-40 exhibits a moderate edge energy and oxidation state, and achieves the highest $E_{1/2}$ of 0.935 V. This phenomenon may stem from the variations in electron transfer between the Fe site and the coordinated carbon matrix, induced by different annealing conditions. A moderate valence state of Fe can balance the adsorption strength of O* intermediates, which is highly favorable for accelerating the overall 4e$^-$ reaction pathway [30]. Subsequently, Fe K-edge Fourier-transformed extended X-ray absorption fine structure (FT-EXAFS) spectra (Fig. 3(d)) were used to analyze key parameters of the synthesized catalysts, including chemical bonds, coordination numbers, bond lengths, and disorder. A range of catalysts display a single peak at approximately 1.5 Å, attributed to the Fe–N scattering path. The absence of Fe–O and Fe–Fe scattering paths suggests that the atomic dispersion of Fe

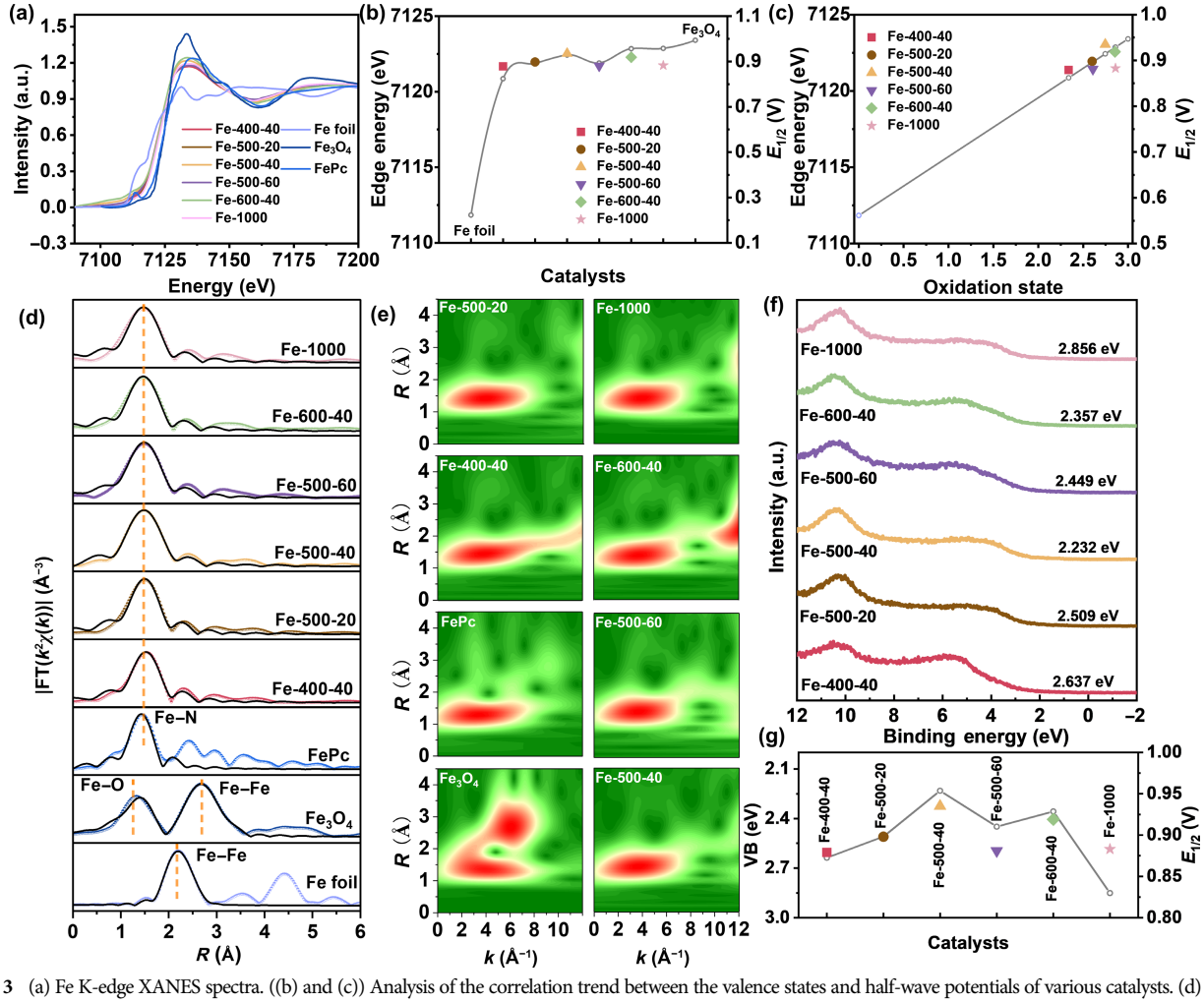


**Figure 3** (a) Fe K-edge XANES spectra. ((b) and (c)) Analysis of the correlation trend between the valence states and half-wave potentials of various catalysts. (d) EXAFS spectra and FT-EXAFS fitting curves. (e) Wavelet transforms of the EXAFS signals. (f) UPS spectra. (g) The relationship between the valence band and half-wave potential of various catalysts.

within these catalysts [31]. Fitting results (Table S1 in the ESM) reveal that Fe-400-40 and Fe-500-60 exhibit configurations of Fe–$N_3$ and Fe–$N_4$, whereas Fe-500-20, Fe-500-40, Fe-600-40, and Fe-1000 predominantly feature the Fe–$N_4$ configuration. Specifically, Fe-500-40 exhibits the shortest Fe–N bond length, indicating a strengthened Fe–N interaction and enhanced stability. Comprehensive analysis of fitting results further reveals that those crucial parameters, such as coordination number, disorder, and Fe–N bond length of the Fe–N–C catalysts, vary significantly with annealing conditions. Wavelet-transform EXAFS (WT-EXAFS) provides both *R*- and *k*-space information, enabling discrimination of backscattering atoms and resolution of overlapping radial distance contributions [32, 33]. As depicted in Fig. 3(e), the maximum contour intensity at approximately 4.1 Å, corresponding to the FT-EXAFS peak at 1.5 Å, can be attributed to the Fe–N bond. Slight differences in the maxima center among catalysts indicate variations in the Fe–N coordination environment [34]. Furthermore, ultraviolet photoelectron spectroscopy (UPS) was used to characterize variations in the valence band edge of the synthetic catalysts. The Fe–N–C catalysts calcined under varying conditions exhibit distinct valence band edges (Fig. 3(f) and Fig. S18 in the ESM). Among them, Fe-500-40 displays the lowest valence band edge, indicating that the density of states (DOS) of the $Fe_1$ sites in Fe-500-40 are most proximate to the Fermi energy level [35]. The lowest valence band edge of Fe-500-40 can be attributed to the interaction between the delocalized π-band of electron-rich carbon and the d-orbitals of $Fe_1$ sites, which enhances the electron density at $Fe_1$ sites [36]. Correlating the valence band edge with the $E_{1/2}$ reveals that Fe-500-40, with the lowest valence band edge, achieves the highest $E_{1/2}$ (Fig. 3(g)). The aforementioned analytical outcomes robustly substantiate that the calcination condition exerts significant control over the atomic coordination and electronic structure of Fe sites, which in turn markedly influences the catalytic activity.

Furthermore, the pivotal role of the carbon matrix in enhancing the performance of Fe–N–C catalysts was thoroughly investigated. In the high-resolution C 1s spectra (Fig. 4(a)), four deconvoluted peaks are observed at 284.8, 285.9, 287.4, and 290.3 eV, corresponding to C–C, C–N, C–O, and C=O bonds, respectively [37, 38]. Notably, the content of $sp^2$ graphitic C species is distinctly evident in Fe-500-40 and Fe-600-60, which may be attributed to an increased content of graphitic C [39]. The high-resolution N 1s spectra (Fig. 4(b)) can be deconvoluted into pyridinic N, M–N (M = Metal), graphitic N, and N-oxide components, with the content of each nitrogen species varying significantly under different calcination conditions (Fig. 4(e)) [40, 41]. As illustrated in Fig. 4(c), the high-resolution O 1s X-ray photoelectron spectroscopy (XPS) spectra reveal four oxygen-containing functionalities: C=O (530.3 eV), M–O (531.7 eV), C–O (533.0 eV), and adsorbed water (534.2 eV) [38, 42]. The contents of these O functionalities display significant variations among Fe–N–C catalysts under different calcination conditions. Moreover, as shown in Fig. 4(d), Raman spectroscopy was employed to elucidate the correlation between the structural characteristics of the carbon matrix and the annealing conditions. The Raman spectra prominently feature two broad peaks at approximately 1340 $cm^{-1}$ (D band) and 1590 $cm^{-1}$ (G band), which serve as indicators for assessing the graphitization degree [43]. To precisely delineate the structure of graphene layers, the overlapping D and G bands were meticulously deconvoluted into four distinct peaks, namely D1, D3, D4, and G [44]. The G band corresponds to the $E_{2g}$ vibrational mode characteristic of pristine $sp^2$ carbon structures without defects. In contrast, the D1

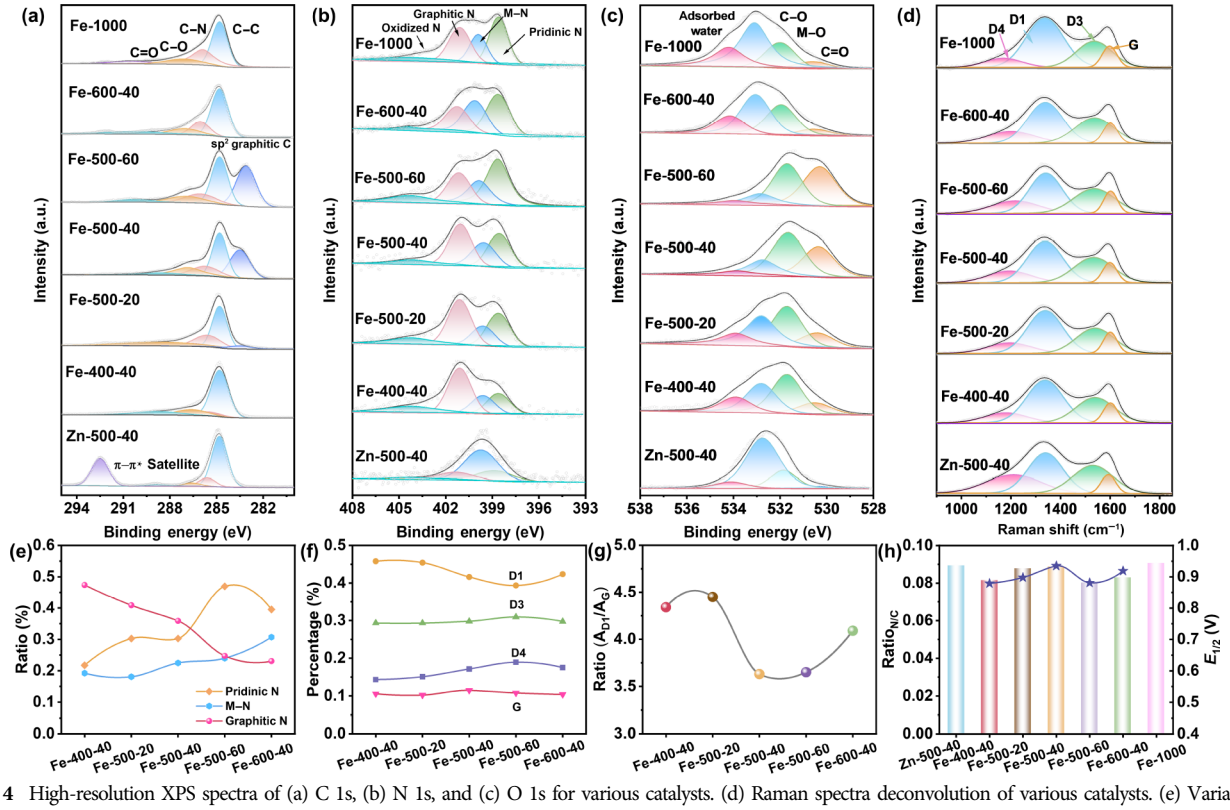


**Figure 4** High-resolution XPS spectra of (a) C 1s, (b) N 1s, and (c) O 1s for various catalysts. (d) Raman spectra deconvolution of various catalysts. (e) Variation of nitrogen species in various catalysts. (f) Variation of carbon species in various catalysts. (g) The ratio of $A_{D1}$ to $A_G$ for various catalysts. (h) Correlation trend between the ratio of N to C and half-wave potential of various catalysts.

band is indicative of the $A_{1g}$ symmetric vibrational mode of graphite domains activated by edge-plane defects. The D3 band, positioned at around 1530 $cm^{-1}$, is associated with amorphous carbon, while the D4 band has been provisionally attributed to the presence of polyene-like species [45, 46]. Fitting results exhibit that the intensities of the D3 and G peaks remain relatively constant across different calcination conditions, whereas the intensities of the D1 and D4 peaks show marked variations with calcination conditions (Fig. 4(f)). The ratio of the D1 to G peak areas ($A_{D1}/A_G$) for various Fe–N–C samples ranges from 3.5 to 4.5 with changing annealing conditions, indicating significant differences in the average graphite domain size and amorphization degree [47, 48]. The differences in probing depth and acquisition conditions between XPS and Raman spectroscopy mean that the degrees of graphitization in Figs. 4(a) and 4(g) are not directly comparable [49]. Notably, Fe-500-40 exhibits the lowest $A_{D1}/A_G$ ratio, signifying a higher degree of graphitization and lower density of edge-plane defects. The contents of C, N, and H were determined via organic elemental analysis, revealing that Fe-500-40 has the highest nitrogen content at 6.323 wt.% (Table S2 in the ESM). Upon correlating the N/C ratios with the $E_{1/2}$ of the catalysts, it is observed that $E_{1/2}$ varies in tandem with fluctuations in the N/C ratio (Fig. 4(h)). Among the examined catalysts, Fe-500-40 exhibits both the highest N/C ratio and $E_{1/2}$. The aforementioned characterization and electrochemical analyses confirmed a strong correlation between the content of nitrogen species and graphitic carbon and catalytic performance, and that modulating graphitic nitrogen content in the carbon framework can significantly enhance the ORR activities of Fe–N–C catalysts.

Through the aforementioned systematic analysis, we have established a close correlation between the catalytic activity and key structural parameters: the atomic coordination and electronic structure of the Fe site, as well as the graphite carbon and nitrogen content in the carbon matrix. To further validate this relationship, we conducted density functional theory (DFT) calculations. These calculations were specifically aimed at elucidating the influence of various adjacent graphitic nitrogen species and the atomic coordination environment of the Fe site on the ORR performance of Fe–N–C catalysts, a series of structural models were constructed, namely Fe–$N_3$–C, Fe–$N_4$–C, Fe–$N_4$–$CN_1$, Fe–$N_4$–$CN_2$, and Fe–$N_4$–$CN_3$ (as shown in Fig. 5(a)). These structural models were constructed from EXAFS fitting results supplemented by XPS, Raman, and organic elemental analysis data. Bader charge analysis revealed electron transfer from the Fe site to the carbon substrate across all models (Fig. 5(b)), indicating distinct interactions between the Fe site and the N-doped carbon matrix [50]. The energy profiles of ORR intermediates adsorbed on these models were assessed (Figs. S19 and S20 in the ESM). Figure 5(c) depicts the Gibbs free energy diagrams for oxygen-containing species adsorption at 1.23 V. All catalysts exhibit a thermodynamically favorable downhill reaction pathway. The final step (*OH + $e^-$ → $OH^-$ + *), identified as the rate-determining step (RDS), shows significant variation in the *OH desorption energy [51]. The desorption energy for *OH release is 2.33 eV for Fe–$N_3$–C and 1.09 eV for Fe–$N_4$–C, respectively. In contrast, the desorption energy of *OH for Fe–$N_4$–$CN_1$, Fe–$N_4$–$CN_2$, and Fe–$N_4$–$CN_3$ is 0.68, 0.69, and 0.66 eV, respectively. These results demonstrate that Fe–$N_4$ coordination reduces the RDS energy barrier far more effectively than Fe–$N_3$ coordination [11, 52]. Moreover, the presence of adjacent graphitic nitrogen species ($CN_1$, $CN_2$, and $CN_3$) further lowers this barrier, accelerating ORR kinetics. The DOS of various Fe–N–C catalysts was calculated (Fig. 5(d) and Fig. S21 in the ESM). The d-band center of Fe–$N_3$–C and Fe–$N_4$–C is located at −1.292 and −1.039 eV, respectively (Fig. 5(d)). In contrast, the d-band centers of Fe–$N_4$–$CN_1$, Fe–$N_4$–$CN_2$, and Fe–$N_4$–$CN_3$ are shifted downward to −0.484, −0.662, and −0.748 eV, respectively. This downward shift indicates that the presence of adjacent graphitic nitrogen species can efficiently optimize the desorption of oxygen-containing intermediates, thereby promoting the continuity of the ORR process [53, 54]. The above calculation results robustly illustrate that the atomic coordination and electronic structure of the Fe site, in conjunction with the content of graphitic nitrogen species within the carbon matrix, can significantly modulate the ORR activity of Fe–N–C catalysts.

## 3 Conclusions

In summary, using Fe-doped ZIF-8 as a precursor, we meticulously regulated the atomic environment of Fe sites and the composition of the carbon matrix through precise temperature programming, thereby synthesizing a series of Fe–N–C catalysts with tailored properties. Among these, the Fe-500-40 catalyst exhibited a high $E_{1/2}$ of 0.935 V and a Tafel slope of 63.69 $mV \cdot dec^{-1}$ in alkaline electrolyte. It also showed excellent anti-methanol and $SCN^-$ performance, with negligible change in $E_{1/2}$ even after 20,000 CV. The Fe-500-40-based ZAB achieved a peak power density of 189.9 $mW \cdot cm^{-2}$ and demonstrated long-term cycling stability. Advanced and systematic characterization elucidates that a moderate valence state of Fe can effectively balance the adsorption strength of O* intermediates, while the electronic configuration of Fe sites is intrinsically linked to the $E_{1/2}$ of ORR. Moreover, the content of N species, graphite carbon, and surface functional groups of the carbon matrix significantly affect catalytic activity. Theoretical calculations further substantiate that both the coordination number of Fe and the presence of graphitic nitrogen species exert a decisive role in regulating the desorption energy of *OH and optimizing the desorption of oxygen-containing intermediates. This work provides a comprehensive and rational illustration for how metal sites and carbon matrix in metal–nitrogen–carbon materials synergistically enhance catalytic activity, offering meaningful guidance for the rational design of metal–support catalysts.

**Electronic Supplementary Material**: Supplementary material (this includes catalyst preparation methods and electrochemical testing, calculation procedures, as well as XRD, SEM, TEM, thermogravimetric analyses, electrochemical data, and computational models) is available in the online version of this article at https://doi.org/10.26599/NR.2026.94908471.

## Data availability

All data needed to support the conclusions in the paper are presented in the manuscript and the Electronic Supplementary Material. Additional data related to this paper may be requested from the corresponding author upon request.

## Acknowledgements

This work was financially supported by the National Major Science and Technology Project of China (No. 2022YFB3807700), the National Natural Science Foundation of China (Nos. 52072217 and

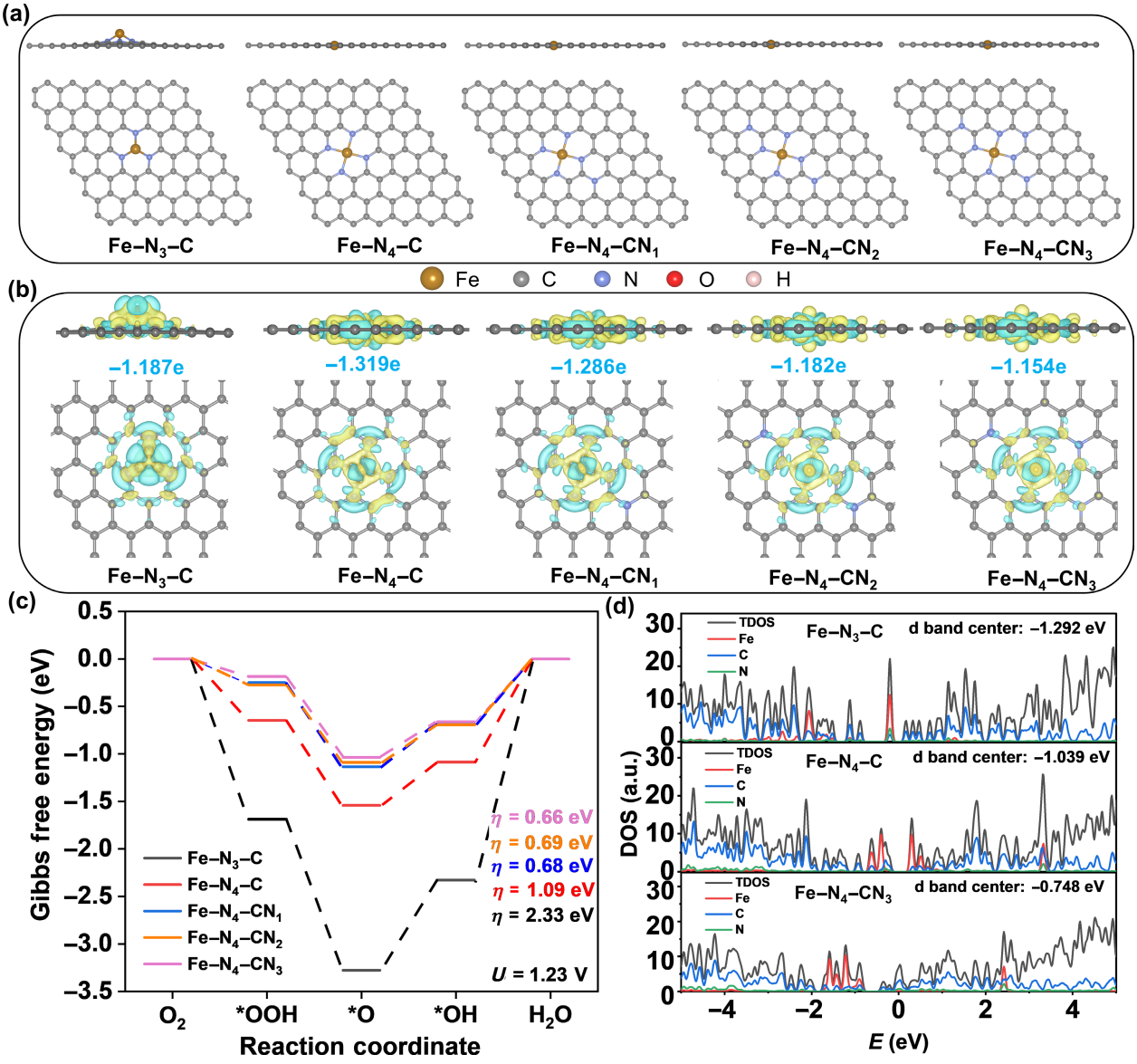


**Figure 5** (a) Structure models of Fe–N–C catalysts. (b) Density difference and the Bader charges are transferred from the Fe site to carbon support. (c) Gibbs free energy diagrams of ORR on different structures at 1.23 V. (d) DOS of various Fe–N–C catalysts.

52172202), the Hubei Provincial Natural Science Foundation Project (Nos. 2024AFB295 and 2024AFB113), Joint Funds of the Hubei Natural Science Foundation Innovation and Development (No. 2022CFD034), the Hubei Natural Science Foundation Innovation Group Project (No. 2022CFA020), and the 10th Young Elite Scientists Sponsorship Program by CAST.

## Declaration of competing interest

All the contributing authors report no conflict of interests in this work.

## Author contribution statement

X. K. D. and H. L. conceived the idea and carried out the experiment. X. L., L.-L. Z., and L. L. evaluated the electrochemical performances. K. Y. and W. B. Z. performed theoretical simulations. X.-L. Y., Z. L., and W. J. M. supervised the whole work. All the authors have approved the final manuscript.

## Use of AI statement

None.

## References

[1] Mehmood, A.; Gong, M. J.; Jaouen, F.; Roy, A.; Zitolo, A.; Khan, A.; Sougrati, M. T.; Primbs, M.; Bonastre, A. M.; Fongalland, D. et al. High loading of single atomic iron sites in Fe–NC oxygen reduction catalysts for proton exchange membrane fuel cells. *Nat. Catal.* **2022**, *5*, 311–323.

[2] Huo, L. P.; Lv, M. H.; Li, M. J.; Ni, X. P.; Guan, J. Y.; Liu, J.; Mei, S. X.; Yang, Y. Q.; Zhu, M. M.; Feng, Q. C. et al. Amorphous $MnO_2$ lamellae encapsulated covalent triazine polymer-derived multi-heteroatoms-doped carbon for ORR/OER bifunctional electrocatalysis. *Adv. Mater.* **2024**, *36*, 2312868.

[3] Lei, H.; Wang, Z. L.; Yang, F.; Huang, X. Q.; Liu, J. H.; Liang, Y. Y.; Xie, J. P.; Javed, M. S.; Lu, X. H.; Tan, S. Z. et al. NiFe nanoparticles embedded N-doped carbon nanotubes as high-efficient electrocatalysts for wearable solid-state Zn–air batteries. *Nano Energy* **2020**, *68*, 104293.

[4] Chen, X.; Feng, P.; Zheng, Y.; Li, H.; Zhang, Y. F.; Shen, Y.; Yan, Y.; Liu, M. K.; Ye, L. Q. Emerging nitrogen and sulfur Co-doped carbon materials for electrochemical energy storage and conversion. *Small* **2025**, *21*, 2412191.
[5] Sawant, K. J.; Zeng, Z. H.; Greeley, J. P. Origin of stability and activity enhancements in Pt-based oxygen reduction reaction catalysts via defect-mediated dopant adsorption. *Angew. Chem.* **2024**, *136*, e202312747.
[6] Chen, Y. Z.; Jin, Z. Y.; Sun, J. L.; Chen, S. L.; Zhang, J. J.; Zhang, S. M. Precise Pt-skin manipulation of strain and ligand effects for oxygen reduction. *eScience* **2025**, *5*, 100396.
[7] Chauhan, M.; Budania, Y.; Modi, A.; Kumar, P.; Pandey, S. K.; Singh, S. Trifunctional nature of heteroatom (B, N, S, O)-doped waste diesel soot: Turning pollutants into potential energy catalysts for HER, OER, and ORR. *Carbon Neutralization* **2025**, *4*, e195.
[8] Wang, S. S.; Zhao, Z. L.; Hu, Y. M.; Jiang, S. P.; Zhang, X. Y. Mesostructured Pt alloy nanotubes with synergistic edge sites as bifunctional electrocatalysts for direct ethanol fuel cells. *Energy Mater.* **2025**, *5*, 500056.
[9] Yin, S. H.; Chen, L.; Yang, J.; Cheng, X. Y.; Zeng, H. B.; Hong, Y. H.; Huang, H.; Kuai, X. X.; Lin, Y. G.; Huang, R. et al. A Fe–NC electrocatalyst boosted by trace bromide ions with high performance in proton exchange membrane fuel cells. *Nat. Commun.* **2024**, *15*, 7489.
[10] Zhao, K. M.; Wu, D. X.; Wu, W. K.; Nie, J. B.; Geng, F. S.; Li, G.; Shi, H. Y.; Huang, S. C.; Huang, H.; Zhang, J. et al. Identifying high-spin hydroxyl-coordinated $Fe^{3+}N_4$ as the active centre for acidic oxygen reduction using molecular model catalysts. *Nat. Catal.* **2025**, *8*, 422–435.
[11] Yu, K.; Guan, S. M.; Zhang, W. B.; Zhang, W. L.; Meng, Y. Y.; Lin, H. J.; Gao, Q. S. Engineering asymmetric electronic structure of Co–N–C single-atomic sites toward excellent electrochemical $H_2O_2$ production and biomass upgrading. *Angew. Chem., Int. Ed.* **2025**, *64*, e202502383.
[12] Zeng, Y.; Zhao, M. T.; Zeng, H L.; Jiang, Q.; Ming, F. W.; Xi, K.; Wang, Z. C.; Liang, H. F. Recent progress in advanced catalysts for electrocatalytic hydrogenation of organics in aqueous conditions. *eScience* **2023**, *3*, 100156.
[13] Shi, X. X.; Wen, Z. L.; Gu, Q. Q.; Jiao, L.; Jiang, H. L.; Lv, H. F.; Wang, H. W.; Ding, J. N.; Lyons, M. P.; Chang, A. et al. Metal–support frontier orbital interactions in single-atom catalysis. *Nature* **2025**, *640*, 668–675.
[14] Chen, C. J.; Wu, Y. L.; Li, X. L.; Ye, Y. T.; Li, Z. L.; Zhou, Y. F.; Chen, J.; Yang, M. Z.; Xie, F. Y.; Jin, Y. S. et al. Modulating Fe spin state in FeNC catalysts by adjacent Fe atomic clusters to facilitate oxygen reduction reaction in proton exchange membrane fuel cell. *Appl. Catal. B: Environ.* **2024**, *342*, 123407.
[15] Teng, X.; Si, D.; Chen, L. S.; Shi, J. L. Synergetic catalytic effects by strong metal–support interaction for efficient electrocatalysis. *eScience* **2024**, *4*, 100272.
[16] Liu, S. Y.; Ning, Y.; Qi, X. R.; Zhao, J. J.; Fu, Y. F.; Zhang, B. Y.; Gao, J.; Miao, J. R.; Song, J. Z.; Huo, Q. CdS-modified ZIF-8-derived porous carbon for organic pollutant degradations under visible-light irradiation. *Res. Chem. Intermed.* **2021**, *47*, 4193–4211.
[17] Yin, S. H.; Yi, H. Y.; Liu, M. L.; Yang, J.; Yang, S. L.; Zhang, B. W.; Chen, L.; Cheng, X. Y.; Huang, H.; Huang, R. et al. An *in-situ* exploration of how Fe/N/C oxygen reduction catalysts evolve during synthesis under pyrolytic conditions. *Nat. Commun.* **2024**, *15*, 6229.
[18] Pandiaraj, S.; Aiyappa, H. B.; Banerjee, R.; Kurungot, S. Post modification of MOF derived carbon via-$gC_3N_4$ entrapment for an efficient metal-free oxygen reduction reaction. *Chem. Commun.* **2014**, *50*, 3363–3366.
[19] Han, Y. C.; Liu, M. L.; Sun, L.; Li, X. C.; Yao, Y. G.; Zhang, C.; Ding, S. Y.; Liao, H. G.; Zhang, L.; Fan, F. R. et al. A general strategy for overcoming the trade-off between ultrasmall size and high loading of MOF-derived metal nanoparticles by millisecond pyrolysis. *Nano Energy* **2022**, *97*, 107125.
[20] Qiu, Z. M.; Li, Y.; Gao, Y. D.; Meng, Z. Y.; Sun, Y. Y.; Bai, Y.; Suen, N. T.; Chen, H. C.; Pi, Y. C.; Pang, H. 2D MOF-assisted pyrolysis-displacement-alloying synthesis of high-entropy alloy nanoparticles library for efficient electrocatalytic hydrogen oxidation. *Angew. Chem., Int. Ed.* **2023**, *62*, e202306881.
[21] Chen, Z. H.; Zhang, L.; Jiang, Y. C.; Su, Z. Y.; Jin, J.; Lei, H.; Yang, X. L. Synergistic electronic and microstructural regulation for high-performance PdPt-based electrocatalysts in the hydrogen evolution reaction. *Chem. Commun.* **2025**, *61*, 8548–8551.
[22] Park, J.; Lee, M.; Feng, D. W.; Huang, Z. H.; Hinckley, A. C.; Yakovenko, A.; Zou, X. D.; Cui, Y.; Bao, Z. N. Stabilization of hexaaminobenzene in a 2D conductive metal–organic framework for high power sodium storage. *J. Am. Chem. Soc.* **2018**, *140*, 10315–10323.
[23] Li, B.; Dai, F.; Xiao, Q. F.; Yang, L.; Shen, J. M.; Zhang, C. M.; Cai, M. Nitrogen-doped activated carbon for a high energy hybrid supercapacitor. *Energy Environ. Sci.* **2016**, *9*, 102–106.
[24] Jiao, L.; Arman, T. A.; Hwang, S.; Fonseca, J.; Okolie, N.; Shaaban, E.; Li, G. H.; Liu, E. S.; Pasaogullari, U.; Babu, S. K. et al. Self-sacrificial template synthesis of Fe–N–C catalysts with dense active sites deposited on a porous carbon network for high performance in PEMFC. *Adv. Energy Mater.* **2024**, *14*, 2303952.
[25] Lei, H.; Wan, Q. X.; Tan, S. Z.; Wang, Z. L.; Mai, W. J. Pt-quantum-dot-modified sulfur-doped NiFe layered double hydroxide for high-current-density alkaline water splitting at industrial temperature. *Adv. Mater.* **2023**, *35*, 2208209.
[26] Streeter, I.; Compton, R. G. Diffusion-limited currents to nanoparticles of various shapes supported on an electrode; spheres, hemispheres, and distorted spheres and hemispheres. *J. Phys. Chem. C* **2007**, *111*, 18049–18054.
[27] Chen, Y. J.; Ji, S. F.; Zhao, S.; Chen, W. X.; Dong, J. C.; Cheong, W. C.; Shen, R. A.; Wen, X. D.; Zheng, L. R.; Rykov, A. I. et al. Enhanced oxygen reduction with single-atomic-site iron catalysts for a zinc–air battery and hydrogen-air fuel cell. *Nat. Commun.* **2018**, *9*, 5422.
[28] Lei, H.; Ma, L.; Wan, Q. X.; Huangfu, Z. W.; Tan, S. Z.; Wang, Z. L.; Mai, W. J. Porous carbon nanofibers confined NiFe alloy nanoparticles as efficient bifunctional electrocatalysts for Zn–air batteries. *Nano Energy* **2022**, *104*, 107941.
[29] Hu, C.; Xing, G. Y.; Han, W. T.; Hao, Y. X.; Zhang, C. C.; Zhang, Y.; Kuo, C. H.; Chen, H. Y.; Hu, F.; Li, L. L. et al. Inhibiting demetalation of Fe–N–C via Mn sites for efficient oxygen reduction reaction in zinc–air batteries. *Adv. Mater.* **2024**, *36*, 2405763.
[30] Asset, T.; Atanassov, P. Iron–nitrogen–carbon catalysts for proton exchange membrane fuel cells. *Joule* **2020**, *4*, 33–44.
[31] Lei, X.; Tang, Q. Y.; Zheng, Y. P.; Kidkhunthod, P.; Zhou, X. L.; Ji, B. F.; Tang, Y. B. High-entropy single-atom activated carbon catalysts for sustainable oxygen electrocatalysis. *Nat. Sustain.* **2023**, *6*, 816–826.
[32] Zhao, S. L.; Tan, C. H.; He, C. T.; An, P. F.; Xie, F.; Jiang, S.; Zhu, Y. F.; Wu, K. H.; Zhang, B. W.; Li, H. J. et al. Structural transformation of highly active metal–organic framework electrocatalysts during the oxygen evolution reaction. *Nat. Energy* **2020**, *5*, 881–890.
[33] Lei, H.; Ma, L.; Wan, Q. X.; Tan, S. Z.; Yang, B.; Wang, Z. L.; Mai, W. J.; Fan, H. J. Promoting surface reconstruction of NiFe layered double hydroxide for enhanced oxygen evolution. *Adv. Energy Mater.* **2022**, *12*, 2202522.
[34] Lei, H.; Huangfu, Z. W.; Chen, L. J.; Yang, X. L.; Wang, Z. L.; Mai, W. J. Structure and defect dual-engineering of cobalt oxides for low-temperature Zn–air batteries. *Nano Res.* **2024**, *17*, 4108–4117.
[35] Guo, L. M.; Wan, X.; Liu, Q. T.; Liu, X. F.; Shang, J. X.; Yu, R. H.; Shui, J. L. Critical role of carbon support in metal nanoaggregate facilitating Fe–N–C catalyst for PEM fuel cell application. *J. Energy Chem.* **2024**, *97*, 669–676.
[36] Sharma, M.; Jang, J. H.; Shin, D. Y.; Kwon, J. A.; Lim, D. H.; Choi, D.; Sung, H.; Jang, J.; Lee, S. Y.; Lee, K. Y. et al. Work function-tailored graphene via transition metal encapsulation as a highly active and durable catalyst for the oxygen reduction reaction. *Energy Environ. Sci.* **2019**, *12*, 2200–2211.

[37] Tang, C.; Wang, B.; Wang, H. F.; Zhang, Q. Defect engineering toward atomic Co–$N_x$–C in hierarchical graphene for rechargeable flexible solid Zn–air batteries. *Adv. Mater.* **2017**, *29*, 1703185.
[38] Miao, Z. P.; Wang, X. M.; Zhao, Z. L.; Zuo, W. B.; Chen, S. Q.; Li, Z. Q.; He, Y. H.; Liang, J. S.; Ma, F.; Wang, H. L. et al. Improving the stability of non-noble-metal M–N–C catalysts for proton-exchange-membrane fuel cells through M–N bond length and coordination regulation. *Adv. Mater.* **2021**, *33*, 2006613.
[39] De Barros Bouchet, M. I.; Martin, J. M.; Avila, J.; Kano, M.; Yoshida, K.; Tsuruda, T.; Bai, S. D.; Higuchi, Y.; Ozawa, N.; Kubo, M. et al. Diamond-like carbon coating under oleic acid lubrication: Evidence for graphene oxide formation in superlow friction. *Sci. Rep.* **2017**, *7*, 46394.
[40] Chen, J. D.; Huang, B. Y.; Cao, R.; Li, L. B.; Tang, X. N.; Wu, B.; Wu, Y. G.; Hu, T.; Yuan, K.; Chen, Y. W. Steering local electronic configuration of Fe–N–C-based coupling catalysts via ligand engineering for efficient oxygen electroreduction. *Adv. Funct. Mater.* **2023**, *33*, 2209315.
[41] Mohd Adli, N.; Shan, W. T.; Hwang, S.; Samarakoon, W.; Karakalos, S.; Li, Y.; Cullen, D. A.; Su, D.; Feng, Z. X.; Wang, G. et al. Engineering atomically dispersed $FeN_4$ active sites for $CO_2$ electroreduction. *Angew. Chem.* **2021**, *133*, 1035–1045.
[42] Roiron, C.; Wang, C.; Zenyuk, I. V.; Atanassov, P. Oxygen 1s X-ray photoelectron spectra of iridium oxides as a descriptor of the amorphous-rutile character of the surface. *J. Phys. Chem. Lett.* **2024**, *15*, 11217–11223.
[43] Sadezky, A.; Muckenhuber, H.; Grothe, H.; Niessner, R.; Pöschl, U. Raman microspectroscopy of soot and related carbonaceous materials: Spectral analysis and structural information. *Carbon* **2005**, *43*, 1731–1742.
[44] Zhang, Q. R.; Tan, X.; Bedford, N. M.; Han, Z. J.; Thomsen, L.; Smith, S.; Amal, R.; Lu, X. Y. Direct insights into the role of epoxy groups on cobalt sites for acidic $H_2O_2$ production. *Nat. Commun.* **2020**, *11*, 4181.
[45] Jiang, P.; Chen, J. T.; Wang, C. L.; Yang, K.; Gong, S. P.; Liu, S.; Lin, Z. Y.; Li, M. S.; Xia, G. L.; Yang, Y. et al. Tuning the activity of carbon for electrocatalytic hydrogen evolution via an iridium–cobalt alloy core encapsulated in nitrogen-doped carbon cages. *Adv. Mater.* **2018**, *30*, 1705324.
[46] Yuan, S.; Zhang, J. W.; Hu, L. Y.; Li, J. N.; Li, S. W.; Gao, Y. N.; Zhang, Q. H.; Gu, L.; Yang, W. X.; Feng, X. et al. Decarboxylation-induced defects in MOF-derived single cobalt atom@carbon electrocatalysts for efficient oxygen reduction. *Angew. Chem., Int. Ed.* **2021**, *60*, 21685–21690.
[47] Xu, Y.; Tu, W. G.; Zhang, B. W.; Yin, S. M.; Huang, Y. Z.; Kraft, M.; Xu, R. Nickel nanoparticles encapsulated in few-layer nitrogen-doped graphene derived from metal–organic frameworks as efficient bifunctional electrocatalysts for overall water splitting. *Adv. Mater.* **2017**, *29*, 1605957.
[48] Perazzolo, V.; Durante, C.; Pilot, R.; Paduano, A.; Zheng, J.; Rizzi, G. A.; Martucci, A.; Granozzi, G.; Gennaro, A. Nitrogen and sulfur doped mesoporous carbon as metal-free electrocatalysts for the *in situ* production of hydrogen peroxide. *Carbon* **2015**, *95*, 949–963.
[49] Qiu, Y. Y.; Fan, D.; Lan, G. J.; Wei, S. H.; Hu, X. J.; Li, Y. Generalized reactivity descriptor of defective carbon catalysts for acetylene hydrochlorination: The ratio of $sp^2$: $sp^3$ hybridization. *Chem. Commun.* **2020**, *56*, 14877–14880.
[50] Wang, N.; Meng, C.; Wang, B.; Tan, X. J.; Wan, Y.; Yang, Y.; Kong, D. Y.; Wang, W. L.; Cao, F. L.; Fielding, A. J. et al. Spin-regulated Fe–N–C catalyst enabled by adjusting coordination nitrogen species for robust oxygen reduction. *Nat. Sci. Rev.* **2025**, *12*, nwaf061.
[51] Lyu, L. L.; Hu, X.; Lee, S.; Fan, W. Q.; Kim, G.; Zhang, J. L.; Zhou, Z.; Kang, Y. M. Oxygen reduction kinetics of Fe–N–C single atom catalysts boosted by pyridinic N vacancy for temperature-adaptive Zn–air batteries. *J. Am. Chem. Soc.* **2024**, *146*, 4803–4813.
[52] Han, J. X.; Bao, H. L.; Wang, J. Q.; Zheng, L. R.; Sun, S. R.; Wang, Z. L.; Sun, C. W. 3D N-doped ordered mesoporous carbon supported single-atom Fe–N–C catalysts with superior performance for oxygen reduction reaction and zinc–air battery. *Appl. Catal. B: Environ.* **2021**, *280*, 119411.
[53] Lei, H.; Zhou, Y. F.; Huangfu, Z. W.; Chen, L. J.; Cao, J.; Yang, X. L.; Mai, W. J.; Wang, Z. L. Noble metal nanoparticles anchored on transition metal phosphides for effective pH-universal hydrogen evolution. *Adv. Sci.* **2025**, *12*, 2504462.
[54] Liu, L. Q.; Rao, X. B.; Zhang, S. M.; Zhang, J. J. Insight into synergy for oxygen reduction electrocatalysis of iron–nitrogen–carbon. *Chem* **2024**, *10*, 1994–2030.